# Non-invasive optoacoustic imaging of dermal microcirculatory revascularization in diet-induced obese mice undergoing exercise intervention

Shan Huang [a,b,1], Hailong He [a,b,1], Robby Zachariah Tom [c,d], Sarah Glasl [a,b], Pia Anzenhofer [a,b], Andre C. Stiel [a,e], Susanna M. Hofmann [c,d,f,*], Vasilis Ntziachristos [a,b,**]

[a] *Institute of Biological and Medical Imaging, Helmholtz Zentrum München, Neuherberg, Germany*
[b] *Chair of Biological Imaging at the Central Institute for Translational Cancer Research (TranslaTUM), School of Medicine and Health, Technical University of Munich, Munich, Germany*
[c] *Institute of Diabetes and Regeneration Research, Helmholtz Zentrum München (GmbH), Neuherberg, Germany*
[d] *Department of Medicine IV, LMU University Hospital, LMU Munich, Munich, Germany*
[e] *University of Regensburg, Faculty for Biology, Regensburg, Germany*
[f] *German Center for Diabetes Research (DZD), Neuherberg 85764, Germany*

## ARTICLE INFO

## ABSTRACT

Microcirculatory dysfunction has been observed in the dermal white adipose tissue (dWAT) and subcutaneous white adipose tissue (scWAT) of obese humans and has been proposed as an early prediction marker for cardio-metabolic disease progression. *In-vivo* visualization and longitudinal monitoring of microvascular remodeling in these tissues remains challenging. We compare the performance of two optoacoustic imaging methods, i.e. multi-spectral optoacoustic tomography (MSOT) and raster-scanning optoacoustic mesoscopy (RSOM) in visualizing lipid and hemoglobin contrast in scWAT and dWAT in a mouse model of diet-induced obesity (DIO) undergoing voluntary wheel running intervention for 32 weeks. MSOT visualized lipid and hemoglobin contrast in murine fat depots in a quantitative manner even at early stages of DIO. We show for the first time to our knowledge that RSOM allows precise visualization of the dWAT microvasculature and provides quantitative readouts of skin layer thickness and vascular density in dWAT and dermis. Combination of MSOT and RSOM resolved exercise-induced morphological changes in microvasculature density, tissue oxygen saturation, lipid and blood volume content in dWAT and scWAT. The combination of MSOT and RSOM may allow precise monitoring of micro-circulatory dysfunction and intervention response in dWAT and scWAT in a mouse model for DIO. Our findings have laid out the foundation for future clinical studies using optoacoustic-derived vascular readouts from adipose tissues as a biomarker for monitoring microcirculatory function in metabolic disease.

## 1. Introduction

Vascularization regulates adipose tissue function [1–3]. Vascular function in adipose tissue is a key factor in metabolic diseases and thus blood vessels are a promising target for overcoming metabolic perturbations associated with obesity [3–7]. As a result, the study of the interplay between vascularization and adipose tissue has attracted increasing attention [8,9]. Non-invasive examination of vascular function *in vivo* in adipose tissues may be suitable as a biomarker for disease

monitoring or for examining treatment efficacy in obesity and related metabolic diseases.

Immunostaining of isolated tissue samples is currently used for *ex vivo* studies of vascularization in adipose tissues in both humans and mice [10–16]. However, this approach is not suitable for longitudinal observations as it requires multiple tissue biopsies or sacrifice. Thus, a non-invasive imaging tool that can visualize and quantify lipids and blood constituents simultaneously or allow repeated assessments of vascular function in a pathological or therapeutic context would be

---

essential for longitudinal monitoring of disease progression and treatment response. Even though non-invasive imaging methods such as Magnetic Resonance Imaging (MRI) [17,18], Computed Tomography (CT) [19–21], and ultrasonograpy [22,23] can visualize the change in adipose tissue volume under physiological, pathological and therapeutic conditions, they require contrast agents for measuring microvasculature or blood volume parameters in adipose tissue, challenging *in vivo* and disseminated applications.

The multi-faceted functions of dermal white adipose tissue (dWAT) have recently drawn much research attention and may also serve as prediction markers for metabolic disease progression [24–28]. It has been observed that vessel density in adipose tissues decreases under obese conditions in mice and humans[5,6]. This phenotype can be rescued by exercising mice [11,12,24,29,30]. Studies that used rodent obesity models to demonstrate the vasculature dysfunction in adipose tissues in obesity[30–32], or its potential as a therapeutic target[3, 33–36], employed end-point assays such as staining or *in vitro* assays to analyze vessel functions. However, such invasive tissue interrogation is not suitable for monitoring vascular changes *in vivo* and longitudinally. Therefore, the effects of obesity-induced vascular dysfunction and the potential for exercise to rescue this phenotype have not been demonstrated in live animals.

In-vivo and longitudinal observations could be enabled by optoacoustic imaging. Optoacoustic visualization can interrogate tissues at the microscopic (~1 mm depth), mesoscopic (<1 cm depth) or macroscopic level (>1 cm depth) and simultaneous deliver anatomical, functional and molecular contrast [37–39]. Within the family of optoacoustic imaging implementations, Multispectral Optoacoustic Mesoscopy (MSOT) operates at the macroscopic regime and can separate spectral contributions of tissue chromophores such as lipids or oxygenated and deoxygenated hemoglobin by multi-wavelength illumination [40,41]. MSOT has been further employed to visualize brown adipose tissue (BAT) and white adipose tissue (WAT) *in vivo* and record BAT activation under cold exposure or drugs in animals and humans [42,43] or the distribution of lipoma and its vascularization [44]. At the mesoscopic regime, Raster-scanning optoacoustic mesoscopy (RSOM) reaches depths of several mm in tissue with resolutions in the 10–30 μm resolution [39,45], much higher than that of MSOT, which is in the range of no less than 100 μm [46]. RSOM has been used to study microvasculature in epidermis and dermis in human skin or assess skin microvasculature changes in patients with diabetics [47].

Herein, we explore for the first time the suitability of optoacoustic methods in the study of adipose tissue and its vascularization and investigate the relative performance of MSOT and RSOM in dWAT imaging. We demonstrate that MSOT can non-invasively image and quantify lipids and blood content in adipose tissues in obese and non-obese mice and as a function of exercise. We recapitulate findings of vascular dysfunction in interscapular BAT (iBAT) and scWAT in diet-induced obesity (DIO) *in vivo* and observe a previously undisclosed decrease in vessel density associated with dWAT in obesity, which can be rescued by exercise. The MSOT findings are confirmed by histology and RSOM and suggest a new role of dWAT vessel density as a possible biomarker for metabolic disease monitoring. In contrast to scWAT that is located deeper in tissue, dWAT sits below the dermis and can be reached by RSOM at a higher resolution than MSOT. Overall, our findings suggest optoacoustic imaging as a suitable method for assessing tissue lipids, vasculature and blood content without contrast agents or endogenous labels. Therefore, the optoacoustic method may facilitate longitudinal and *in-vivo* animal research and drug development and has the potential to be clinically applied for *in vivo* monitoring of metabolic biomarkers.

## 2. Methods

**Multi-spectral Optoacoustic Tomography and image analysis.** MSOT measurements were performed using a 256-channel real-time imaging system (inVision 256, iThera Medical, Germany). The detailed information of the system has been reported in our previous work[40,48]. For the mice measurements, 27 optical wavelengths in the range of 700–960 nm with step of 10 nm were applied to collect multi-spectral optoacoustic signals by using an optical parametric oscillator laser with a 50 Hz repetition rate. The optoacoustic signals were averaged 10 times at each wavelength during data acquisition. For in vivo mice measurements, animals were anaesthetized by continuous inhalation of 2 % isoflurane (vaporized in 100 % oxygen at 0.8 l/min) and subsequently placed within an animal holder in a supine position relative to the transducer array. The animals were kept into a thin, clear, polyethylene membrane and positioned in the water bath maintained at 34 degrees, which provided acoustic coupling and maintained animal temperature while imaging. The detailed procedure of handing mice in the MSOT imaging system was clearly described in our previous work [40,48]. MSOT data were analysed by ViewMSOT software (v3.8, *iThera* Medical, Munich, Germany). MSOT images were reconstructed using the model linear method. For unmixing of Hb, HbO2, Lipid, H2O, and ICG, a linear regression method was used to fit the acquired data and estimate the constituent spectra and their proportion distribution[48]. Each unmixing data point for statistics was averaged from three ROIs in the same subject.

**Histopathology.** Adipose tissue specimen were sampled according to established organ sampling and trimming guidelines for rodent animal models [49]. The samples were fixed in neutrally-buffered 4 % formaldehyde solution for 24 hours and subsequently routinely embedded in paraffin. 3 μm thick sections were stained with haematoxylin and eosin (HE), using a HistoCore SPECTRA ST automated slide stainer (Leica, Germany) with prefabricated staining reagents (Histo-Core Spectra H&E Stain System S1, Leica, Germany), according to the manufacturer's instructions. Histopathological examination was performed by a pathologist in a blinded fashion (*i.e.,* without knowledge of the treatment-group affiliations of the examined slides).

**RSOM imaging and data analysis.** The present study used an in-house portable RSOM imaging system featuring a transducer with central frequency of 50 MHz, which has been described in detail elsewhere [50,51]. An Onda laser (Bright Solutions, Italy) with dimensions of $19{\times}10{\times}9$ cm3 was used to provide light with wavelength of 532 nm. The repetition rate of the laser was 1 kHz, yielding an optical fluence of 3.75 μJ/mm2 under the safety limit. The anaesthetized mouse was placed onto a bed and into a warmed water bath, with the scanned region under the water level and the head above the water level. An optically and acoustically transparent plastic membrane was affixed using surgical tape on the mouse skin at the scanned region. The scanning head containing the laser output and transducer was brought close to the membrane to position the focal point of the ultrasound detector slightly above the skin surface and thereby maximize detection sensitivity. The scanning head contained water as coupling medium. Two mechanical stages (PI, Germany) were used to scan the RSOM head. The laser and controller of the mechanical stages were both stored inside a plastic case, which ensured laser safety. The scanning field of view is $4{\times}2$ mm$^2$ with step size 7.5 μm in the fast axis and 15 μm in the slow axis. The total scanning time of one measurement took about 70 s. For image reconstruction, optoacoustic signals were separated into lower (10–40 MHz, red) and higher (40–120 MHz, green) frequencies to distinguish larger (diameter of 50 to more than 100 μm) and smaller (diameter of 10–40 μm) vessels, respectively. This bandwidth separation was performed for all RSOM dataset using the same method by using the same frequency ranges, meaning that larger (red encoded) and smaller (green encoded) vessels represent the same size range throughout all mice measurements. The two reconstructed images $R_{low}$ and $R_{high}$ corresponded to the low- and high frequency bands. A composite image was constructed by fusing $R_{low}$ into the red channel and $R_{high}$ into the green channel of a same RGB image. The detail process has been introduced in our previous work [50].

To compute dWAT thickness, RSOM images were first flatted based on our surface detection approach [52]. The reconstructed volume of selected frequency band (10–40 MHz) was split into four stacks with 0.5 mm thickness along the slow scanning axis. Then, the dermis layer in the MIP image of each stack were automatically segmented by graph theory and dynamic programming-based approach [53]. The thickness of the dermis layer was calculated as the average width of the four segmented boundaries. The dermis layer was segmented as starting from the bottom boundary of the dermis layer and further extending 1 mm depth. In the $4\times2$ mm scanning region, the vessel density in the segmented dermis layer was calculated as $N \times dV$, where N represents the number of voxels with intensity above 20 % of the maximum voxel intensity, and $dV$ is the voxel volume.

**Mouse studies**. Age-matched male mice (Jackson laboratory; strain # **B6(Cg)-*Tyr*$^{c-2\,J}$/J**) were divided into chow Altromin 1310; 14 kcal% fat, 59 kcal% carbohydrates) and high fat-diet (HFD); D12331; 58 kcal% fat and 25.5 kcal% sucrose, Research Diet, New Brunswick, NJ, USA) groups. Each SD and HFD groups were further divided into either sedentary control group or exercise group. The exercise group had free access to voluntary wheels within their home cage. The wheel running profile (Figure S7) which includes time, duration, and speed was monitored using a commercially available wifi wheel running system (Low-Profile Wireless Running Wheel, Med associates inc, St. Albans, VT 05478, US). To avoid social stress, two mice per cage were housed throughout the duration of the study). At the end of the study, mice were euthanized with over dose of ketamine and xylazine and blood and organs were collected. The animal studies were approved and conducted in accordance with the Animal Ethics Committee of the government of Upper Bavaria, Germany.

**Statistics.** Data were analyzed using GraphPad Prism (v. 8.4.2; GraphPad Software, La Jolla, CA). All data presented as mean $\pm$ SEM unless otherwise stated. Group size (n) is indicated for each experiment in figure legends. Student's t-test was used for comparisons of two independent groups. One-way ANOVA followed by Tukey's post hoc test was used for comparing more than two independent groups. A p-value of $< 0.05$ was considered as statistically significant. Significant digit: *P$<$ 0.05, **P$<$ 0.01, *** P$<$ 0.001.

## 3. Results

### 3.1. MSOT of lipid, total blood volume and tissue oxygenation of scWAT and iBAT in lean male mice

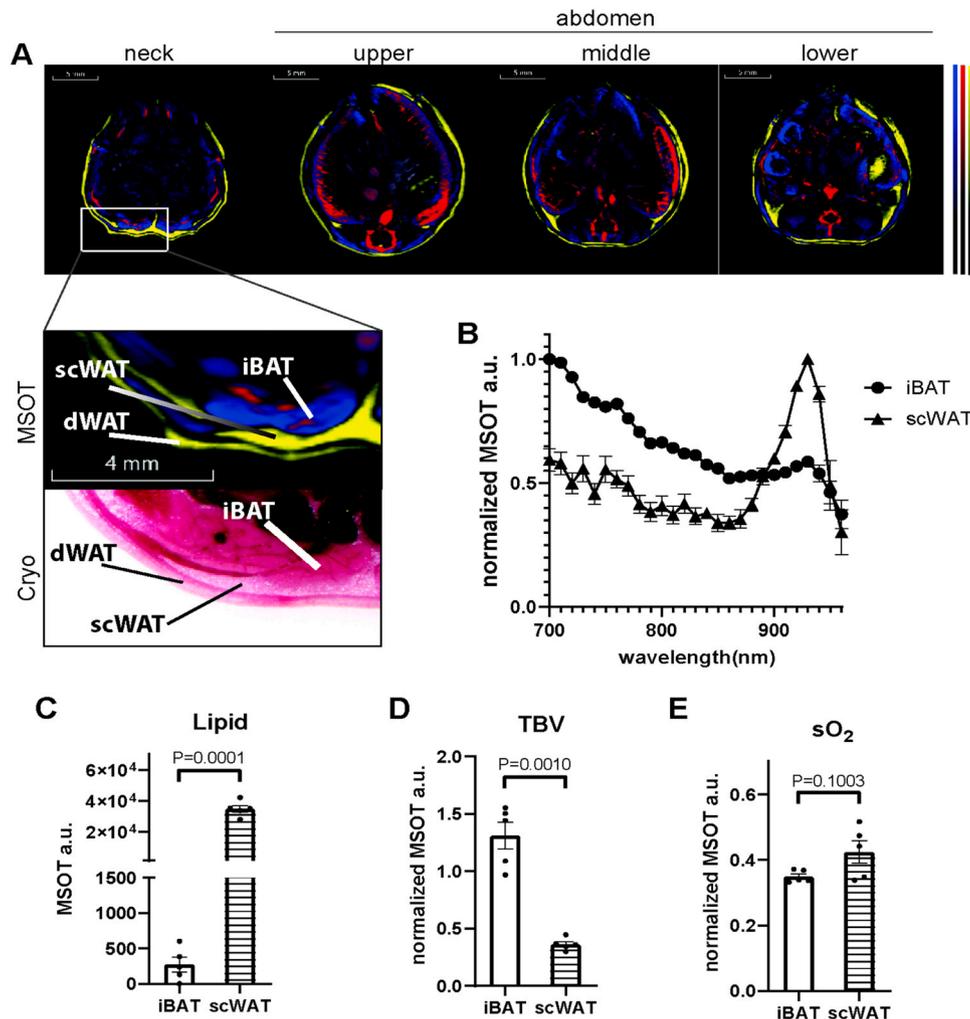MSOT (Fig. 1A) identified three distinct fat depots, iBAT, scWAT and



**Fig. 1.** MSOT imaging of brown adipose tissue (BAT) and white adipose tissue (WAT) *in vivo*. A. Reconstructed MSOT image (800 nm) with linear unmixing data in neck, upper, middle and lower abdominal area. Higher magnitude images are showing neck region with anatomical reference from cryo section image. Unmixing result: blue for Hb (deoxy-haemoglobin), red for HbO$_2$ (oxy-haemoglobin), yellow for lipid. The color bar shows the color coding of MSOT a.u. from minimum to maximum (bottom to top). B. For visualization purposes spectra are normalized to maxima. Spectra of interscapular brown adipose tissue (iBAT) and subcutaneous white adipose tissue (scWAT). n = 5. C. Unmixing result of lipid from iBAT and scWAT, n = 5. D. Total blood volume (TBV) results from iBAT and scWAT, n = 5. E. Tissue oxygenation (sO$_2$) results from iBAT and scWAT, n = 5. dWAT: dermal white adipose tissue.

dWAT in the neck region of mice (Fig. 1A, lower panel). To verify that MSOT can distinguish BAT from WAT, we acquired spectral data in the 700 nm to 960 nm range from regions of expected iBAT and scWAT (Fig. 1B) and then unmixed the signals determining the lipid, oxygenated hemoglobin and deoxygenated hemoglobin content. Already from a qualitative inspection of the mean spectra (mean over area and N=5 mice) between 700 nm and 880 nm, the lipid peak at 930 nm is relatively more prominent in the case of scWAT suggesting higher lipid content. In contrast relative signals of the spectral region corresponding to hemoglobin absorption was more pronounced for iBAT suggesting higher vascularization relative to lipid. Using the spectral data, we unmixed the lipid and blood contents in scWAT and iBAT. As suggested by the spectra shown in Fig. 1C, scWAT contained significantly more lipid than iBAT, while iBAT exhibited a higher total blood volume (TBV) than scWAT (Fig. 1D). Tissue oxygenation ($sO_2$) readout measured by MSOT revealed that $sO_2$ rates between iBAT and scWAT were similar (Fig. 1E).

### 3.2. MSOT of lipid and blood content in murine fat depots at the onset of DIO

Following the MSOT assessment of adipose tissue in male mice fed with standard diet (SD), we studied whether MSOT could monitor obesity-mediated pathological changes in adipose tissues in a DIO mouse model. Male mice were fed high fat diet (HFD) or chow for 3 months. The body weight of HFD-fed mice was significantly higher than SD-fed mice (Figure S1A). The weight of gonadal fat (gWAT), a visceral fat depot, inguinal fat (ingWAT) and a scWAT depot were all increased in HFD fed-mice, confirming a DIO phenotype (Figure S1 B-D). Consistently, MSOT measurements revealed an increase in lipid content in both iBAT and scWAT upon HFD feeding compared to chow feeding (Fig. 2A). To enhance the visualization and relative comparison of spectral features, we normalized all tissue spectra to the highest OA signal acquired in the 700–960 nm range (Figs. 2B and 2C). Qualitative inspection of the spectra, especially the relative contributions of regions from lipid absorption (930 nm) and hemoglobin (680–900 nm), of iBAT from HFD-fed mice showed a much more prominent lipid peak at 930 nm compared to chow-fed mice, indicating a higher lipid content (Fig. 2B). In contrast, the change in scWAT spectra caused by DIO was less obvious (Fig. 2C). After spectral unmixing, the lipid content readout from iBAT showed significant increase in DIO mice compared to lean mice, indicating an ectopic accumulation of lipid in the tissue (Fig. 2D, E). This observation was consistent with our histology findings showing larger fat vacuoles in iBAT from DIO mice, as compared to lean mice (Figure S2A). By quantifying the coverage of fat area from histological images, we found that iBAT from DIO mice has higher fat coverage than that from lean mice (Figure S2B). Compared to iBAT, we observed a less obvious change in the spectral composition in scWAT upon HFD feeding (Fig. 2F). The total blood volume in both iBAT and scWAT were all decreased in DIO mice (Fig. 2G, H, I). These findings were consistent with findings from other studies using end point *ex vivo* methods[5,6]. Even with one month of HFD feeding, similar results were obtained using MSOT in the same cohort, which indicates that vessel function was already altered, albeit to a lesser extent (Figure S3).

### 3.3. Combination of MSOT and RSOM visualizes and quantifies accurately exercise-induced morphological changes in vessel density, tissue oxygen saturation, lipid and blood content of dWAT and scWAT

After showing that MSOT accurately detects morphological changes in iBAT and scWAT of DIO mice, we determined whether exercise-induced modulation in adipose tissue mass and function can be monitored by MSOT. As expected HFD fed male and female mice under sedentary conditions exhibited significantly higher body weights compared to sedentary chow diet fed mice. Exercise reduced body weights exclusively in HFD-fed male mice to that of chow-fed male mice, indicating a rescue of a DIO phenotype (Figure S4). In addition to iBAT

and scWAT, we also analysed dWAT in these cohorts. The absorption spectrum of dWAT was similar to scWAT (Fig. 1B, S4). To analyse dWAT in the mouse body, we calculated the percentage of dWAT in the skin, which consists of the epidermis, dermis and hypodermis (dWAT) by MSOT and compared it to the percentage of dWAT in the skin calculated by 2D histology in order to validate our MSOT findings. Using MSOT, we also performed tissue content analysis for TBV to determine blood perfusion in the tissue. In parallel, we performed RSOM imaging to measure dWAT thickness and to visualize the vasculature in the different layers of the skin including dWAT. To validate our vascular readouts from MSOT and RSOM, we performed immunohistochemical staining for CD31 on skin tissue slices, a marker commonly used to demonstrate the presence of endothelial cells in histological tissue sections [54], and quantified the CD31 positive area (Fig. 3A). Our MSOT measurements revealed a significant increase of dWAT percentage in the skin of HFD fed male and female mice compared to chow fed mice (Fig. 3A-C; S1D). This finding was consistent with results obtained by an independent MRI measurement study [55]. Voluntary wheel running exercise restored dWAT volume in HFD-fed male mice to normal levels (Fig. 3A, B) in contrast to female mice where no significant changes in dWAT volume were detected after exercise (Fig. S4). Our MSOT findings were consistent with the skin histology of HFD and chow fed mice (Fig. 3A, C). RSOM was also able to detect HFD-induced thickening of dWAT as well as the exercise-induced reduction in dWAT thickness in male mice only. In female HDF-fed mice exercise did not change the thickness of dWAT (Fig. 3A, D; S4). We then measured TBV by optoacoustic methods and validated our findings by analysing the CD31+ area coverage by immunohistochemical staining in the dermis and dWAT (hypodermis) layer of the skin (Fig. 3E-G, S6). We found that in dWAT, TBV measured by MSOT was significantly decreased in sedentary HFD-fed mice and this phenotype was rescued by voluntary exercise in male mice only (Fig. 3E). This increase in exercise-induced vascular density in HFD-fed male mice was confirmed by our histological staining. However, our histological CD31 based analysis did not confirm the significant decrease in vascular density in HFD-fed mice compared to chow fed mice that we observed by MSOT (Fig. 3F). We assume that this inconsistence is a result of comparing a two-dimensional output (area by CD31+staining) with the three-dimensional output (blood volume by MSOT). RSOM measurements detected a DIO-induced decrease of vessel density and the restoration of the latter by exercise in male mice (Fig. 3G). Exercise did not affect vessel density in the dermis of female mice (Fig S4). In contrast to dWAT, dermis had no change in CD31+ area coverage measured by histology and vessel density measured by RSOM, indicating an unaltered vascular function in dermis in DIO mice no matter whether they underwent voluntary running or not (Figure S6). MSOT was not employed for dermis analysis because of the limitation of resolution.

### 4. Discussion

In this study, we verified that MSOT can visualize and quantify lipid and blood contents in various adipose tissues, including iBAT, scWAT and dWAT of mice. For the first time to our knowledge, we observed *in vivo* that scWAT and iBAT exhibit a decrease in vascularization when DIO occurs [5,6]. Our non-invasive *in vivo* measurements replicate earlier findings by others using invasive *ex-vivo* and end-point *ex vivo* methods. Our approach allows repetitive and longitudinal non-invasive monitoring of vascular function in adipose tissues undergoing patho-physiological processes *in vivo*, including, but not limited to, DIO associated microvascular disease. In this study, we applied a preclinical version of MSOT modality. Although the clinical MSOT device shares the same principles with the preclinical MSOT device we used herein, the measurement and the quantification procedure need to be adjusted for human subjects, in which the depth of targeted tissue is different from mice.

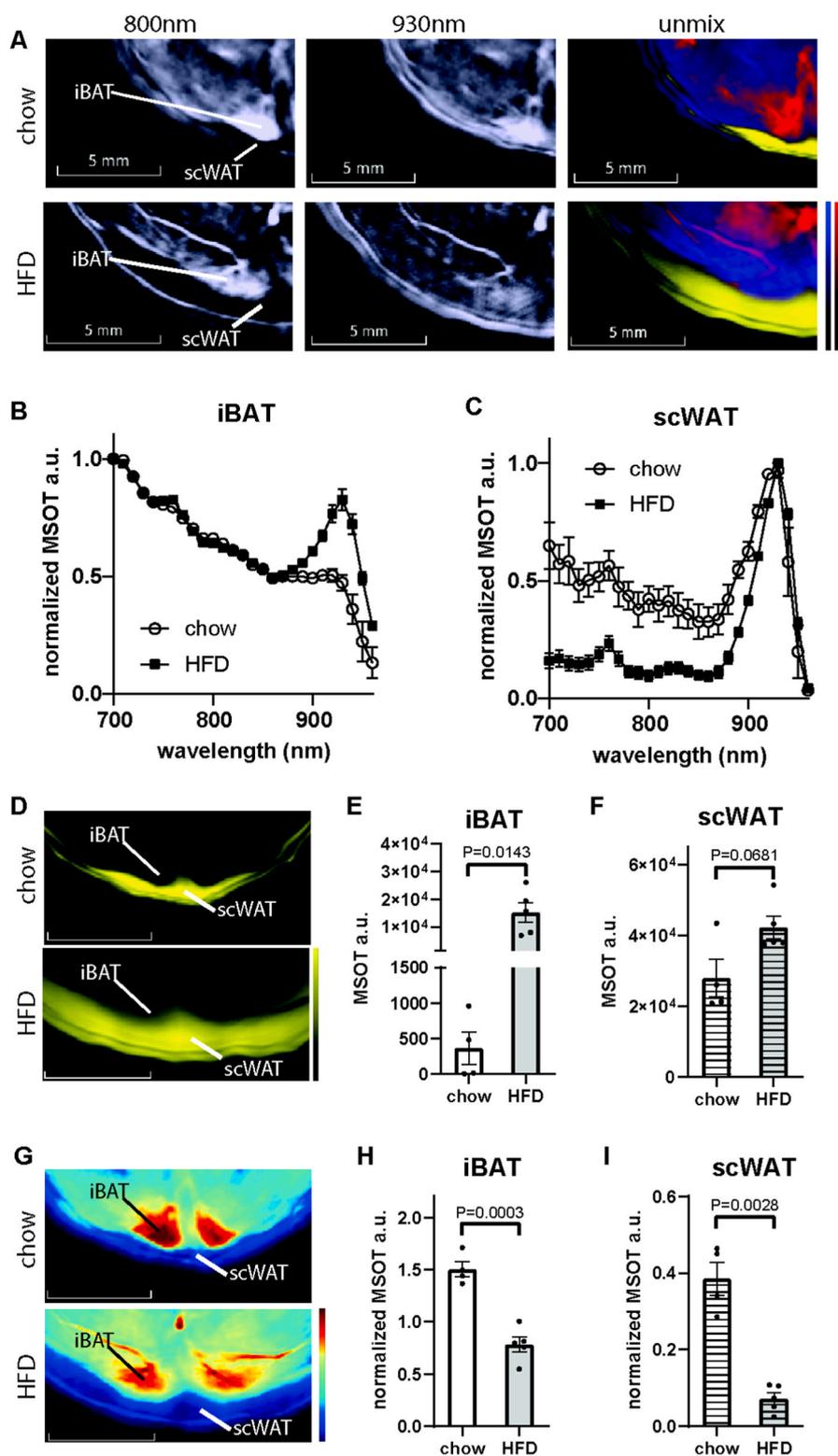Here we found that MSOT can provide a quantitative readout for

**Fig. 2.** Comparison of blood and lipid content of BAT and scWAT between healthy and DIO mice using MSOT imaging. A. Reconstructed MSOT image (800 nm) with linear unmixing data of Hb, HbO$_2$, and lipid from chow and high fat diet (HFD)-fed mice. The color bar shows the color coding of MSOT a.u. from minimum to maximum (bottom to top). B-C. For visualization purposes spectra are normalized to maxima. Spectra of BAT (B) and scWAT (C) from chow and HFD-fed mice. Healthy: n = 4, obese: n = 5. D. MSOT image of lipid unmixing from chow and HFD-fed mice. The color bar shows the color coding of MSOT a.u. from minimum to maximum (bottom to top). E-F. Unmixing result of lipid from BAT (E) and scWAT (F). G. MSOT image of TBV unmixing from chow and HFD-fed mice. The color bar shows the color coding of MSOT a.u. from minimum to maximum (bottom to top). H-I. Unmixing result of TBV from BAT (H) and scWAT (I).
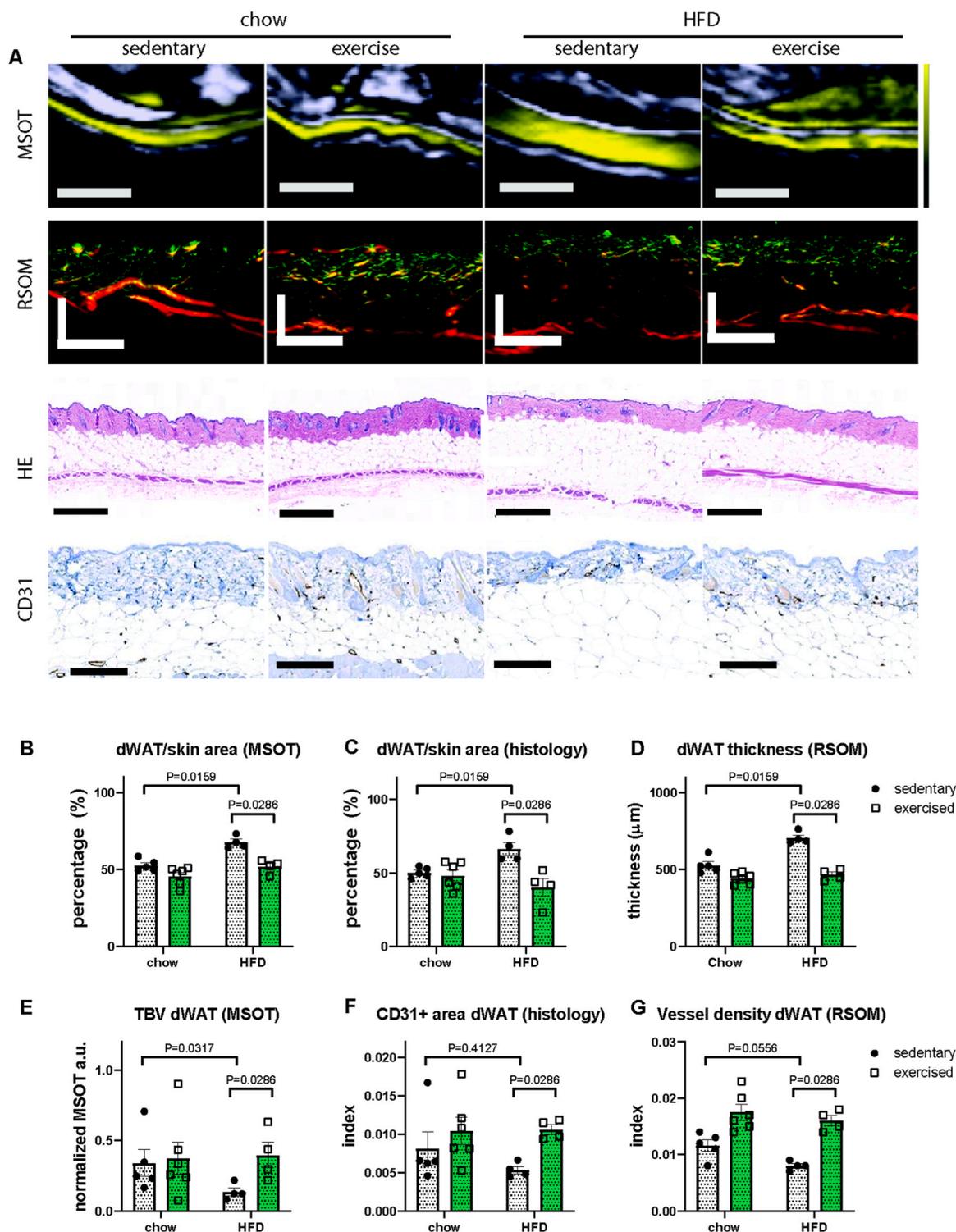
**Fig. 3.** Comparison of dermal adipose tissue (dWAT) characteristic in chow and HFD-fed mice with or without exercise. A. MSOT, RSOM, HE and CD31 staining images from chow and HFD-fed mice with or without exercise. Scale bar: MSOT 2 mm, RSOM 500 μm, HE 500 μm, CD31 200 μm. The RSOM images are color-coded to represent the two reconstructed frequency bands (red: larger structures in the bandwidth of 10–40 MHz; green: smaller structures in the bandwidth of 40–120 MHz). B-C, Percentage of dWAT in skin calculated from MSOT (B) and histology (C). D. dWAT thickness measured by RSOM. E. TBV in dWAT results measured by MSOT. F. CD31+ area coverage index in whole dWAT. G. TBV in dWAT results measured by RSOM. For data in B, C, E, F, Chow sedentary: n = 5, chow exercised: n = 6, HFD sedentary: n = 4, HFD exercised: n = 4. For data in D and G, each group n = 5.

blood volume in the tissue, but at the same time it does not allow visualization of small vessels due to insufficient resolution. To study the morphological changes in tissue vasculature, RSOM is a better choice of optoacoustic method compared to MSOT. It is important to note that RSOM can only reach about 5 mm depth in mouse tissue. Thus, RSOM is more suitable than MSOT for the study of dWAT, but not of iBAT or scWAT. Besides the visualization of morphological changes in the vasculature of the skin, which cannot be achieved by MSOT, RSOM can also provide quantitative readout of skin layer thickness, vascular density of different skin layers including dWAT (hypodermis) and dermis.

The latter may be of critical importance for the accurate assessment of treatment success in diabetic patients suffering from skin frailty and impaired wound healing. In this study, we only employed one wavelength for RSOM imaging allowing the visualization of blood. Since this wavelength does not allow lipid visualization, the identification of dWAT was based on vessel density, which is much lower in dWAT as compared to the attached dermal layer. However, a multi-spectra method has been recently developed for RSOM technology that will allow visualization of multiple contrasts in the tissue including lipid in future studies[56]. By using this multi-wavelength RSOM approach, measurements of dWAT will facilitate a precise skin layer analysis.

Monitoring dWAT vascular function in physiological and pathological conditions, such as hair growth and wound healing, will provide valuable information on morphological changes in these processes, and most importantly provide tools to assess treatment response to vasculature-targeting drugs. For example, there is recent evidence that after depilation, HFD fed mice have a delayed entry into anagen phase in hair growth, in which hair follicles are in contact with dWAT to gain nourishment from dWAT's blood supply [27]. Our observations on dWAT vascular dysfunction under DIO conditions may contribute to further understand as how obesity may affect hair growth.

Clinical applications of optoacoustic imaging are rapidly emerging. Studies using clinical MSOT and RSOM indicated a great potential of these optoacoustic modalities for diagnosing skin diseases, vascular diseases, inflammatory diseases, and cancer [57]. However, these applications are mainly taking the advantage of optoacoustic imaging in visualization and quantification of blood content in the tissue and tissue metabolism since the dominant endogenous contrast in most of the tissues is from haemoglobin. In this study, we applied optoacoustic imaging to visualize and quantify lipid and blood content simultaneously to monitor pathological changes in adipose tissues under DIO conditions. Furthermore, we found that voluntary running exercise rescues vascular dysfunction caused by DIO in male mice in contrast to female mice. Our findings set up a base for future clinical studies using optoacoustic-derived vascular readouts from adipose tissues as a biomarker for the personalized monitoring of vascular function in response to stimuli or therapy.

## CRediT authorship contribution statement

**Andre C. Stiel:** Conceptualization. **Susanna Hofmann:** Writing – review & editing, Project administration, Funding acquisition, Conceptualization. **Sarah Glasl:** Data curation. **Pia Anzenhofer:** Data curation. **Vasilis Ntziachristos:** Writing – review & editing, Supervision, Project administration, Funding acquisition, Conceptualization. **Hailong He:** Writing – review & editing, Writing – original draft, Visualization, Methodology, Investigation, Formal analysis, Data curation, Conceptualization. **Robby Zachariah Tom:** Writing – review & editing, Resources, Formal analysis. **Shan Huang:** Writing – original draft, Methodology, Formal analysis, Data curation, Conceptualization. SH conceived the study, designed, and performed the experiments, analysed the data and wrote the manuscript. HH conceived the study, designed, and performed the experiments, analysed the data, and wrote the manuscript. RZT performed the experiments, analysed the data, and wrote the manuscript. SG performed the in vivo experiments. PA performed the in vivo experiments. ACS conceived the study. SMH conceived the study and wrote the manuscript. VN conceived the study and wrote the manuscript..

## Declaration of Competing Interest

The authors declare the following financial interests/personal relationships which may be considered as potential competing interests:V. N. is an equity owner and consultant for iThera Medical GmbH, Munich, Germany. If there are other authors, they declare that they have no known competing financial interests or personal relationships that could

have appeared to influence the work reported in this paper

## Data Availability

Data will be made available on request.

## Acknowledgements

## Appendix A.  Supporting information

Supplementary data associated with this article can be found in the online version at doi:10.1016/j.pacs.2024.100628.

## References

[1] M.A. Rupnick, et al., Adipose tissue mass can be regulated through the vasculature, Proc. Natl. Acad. Sci. USA vol. 99 (16) (Aug 6 2002) 10730–10735, https://doi.org/10.1073/pnas.162349799.

[2] J. Ye, Adipose tissue vascularization: its role in chronic inflammation, Curr. Diab Rep. vol. 11 (3) (Jun 2011) 203–210, https://doi.org/10.1007/s11892-011-0183-1.

[3] Y. Cao, Adipose tissue angiogenesis as a therapeutic target for obesity and metabolic diseases, Nat. Rev. Drug Discov. vol. 9 (2) (Feb 2010) 107–115, https://doi.org/10.1038/nrd3055.

[4] G. Martinez-Santibanez, K.W. Cho, C.N. Lumeng, Imaging white adipose tissue with confocal microscopy, Methods Enzym. vol. 537 (2014) 17–30, https://doi.org/10.1016/B978-0-12-411619-1.00002-1.

[5] M. Graupera, M. Claret, Endothelial cells: new players in obesity and related metabolic disorders, *Trends Endocrinol Metab.* vol. 29 (11) (nov 2018) 781–794, https://doi.org/10.1016/j.tem.2018.09.003.

[6] P. Trayhurn, Hypoxia and adipose tissue function and dysfunction in obesity, Physiol. Rev. vol. 93 (1) (Jan 2013) 1–21, https://doi.org/10.1152/physrev.00017.2012.

[7] K. Sun, C.M. Kusminski, P.E. Scherer, Adipose tissue remodeling and obesity, J. Clin. Invest vol. 121 (6) (Jun 2011) 2094–2101, https://doi.org/10.1172/JCI45887.

[8] M.W. Laschke, T. Spater, M.D. Menger, Microvascular Fragments: More Than Just Natural Vascularization Units, *Trends Biotech*nol vol. 39 (1) (Jan 2021) 24–33, https://doi.org/10.1016/j.tibtech.2020.06.001.

[9] G. Hutchings, et al., The proliferation and differentiation of adipose-derived stem cells in neovascularization and angiogenesis, Int J. Mol. Sci. vol. 21 (11) (May 27 2020), https://doi.org/10.3390/ijms21113790.

[10] J.B. Seo, et al., Knockdown of Ant2 Reduces Adipocyte Hypoxia And Improves Insulin Resistance in Obesity, Nat. Metab. vol. 1 (1) (Jan 2019) 86–97, https://doi.org/10.1038/s42255-018-0003-x.

[11] S.Y. Min, et al., Exercise Rescues Gene Pathways Involved in Vascular Expansion and Promotes Functional Angiogenesis in Subcutaneous White Adipose Tissue, Int J. Mol. Sci. vol. 20 (8) (Apr 25 2019), https://doi.org/10.3390/ijms20082046.

[12] S. Kolahdouzi, E. Talebi-Garakani, G. Hamidian, A. Safarzade, Exercise training prevents high-fat diet-induced adipose tissue remodeling by promoting capillary density and macrophage polarization, Life Sci. vol. 220 (Mar 1 2019) 32–43, https://doi.org/10.1016/j.lfs.2019.01.037.

[13] M. Spencer, et al., Adipose tissue extracellular matrix and vascular abnormalities in obesity and insulin resistance, *J. Clin. Endocrinol Metab.* vol. 96 (12) (Dec 2011) E1990–8, https://doi.org/10.1210/jc.2011-1567.

[14] M. Pasarica, et al., Reduced adipose tissue oxygenation in human obesity: evidence for rarefaction, macrophage chemotaxis, and inflammation without an angiogenic response, Diabetes vol. 58 (3) (Mar 2009) 718–725, https://doi.org/10.2337/db08-1098.

[15] Y. Tong, Y. Zhang, Z. Shan, Y. Xu, X. Gao, W. Yao, Improving high-fat diet-induced obesity and fatty liver by adipose tissue targeted delivery of vascular endothelial growth factor-B, Life Sci. vol. 253 (Jul 15 2020) 117677, https://doi.org/10.1016/j.lfs.2020.117677.

[16] Y. Xue, S. Lim, E. Brakenhielm, Y. Cao, Adipose angiogenesis: quantitative methods to study microvessel growth, regression and remodeling in vivo, Nat. Protoc. vol. 5 (5) (May 2010) 912–920, https://doi.org/10.1038/nprot.2010.46.

[17] S.A. Gronemeyer, R.G. Steen, W.M. Kauffman, W.E. Reddick, J.O. Glass, Fast adipose tissue (FAT) assessment by MRI, Magn. Reson Imaging vol. 18 (7) (Sep 2000) 815–818, https://doi.org/10.1016/s0730-725x(00)00168-5.

[18] H.H. Hu, H.E. Kan, Quantitative proton MR techniques for measuring fat, NMR Biomed. vol. 26 (12) (Dec 2013) 1609–1629, https://doi.org/10.1002/nbm.3025.

[19] J. Mrzilkova, et al., Morphology of the vasculature and blood supply of the brown adipose tissue examined in an animal model by micro-CT, Biomed. Res Int vol. 2020 (2020) 7502578, https://doi.org/10.1155/2020/7502578.

[20] P. Marzola, F. Boschi, F. Moneta, A. Sbarbati, C. Zancanaro, Preclinical in vivo imaging for fat tissue identification, quantification, and functional characterization, Front Pharm. vol. 7 (2016) 336, https://doi.org/10.3389/fphar.2016.00336.

[21] C.L. Schlett, U. Hoffmann, [Identification and quantification of fat compartments with CT and MRI and their importance], Radiologe vol. 51 (5) (May 2011) 372–378, https://doi.org/10.1007/s00117-010-2088-4.

[22] A. Bazzocchi, G. Filonzi, F. Ponti, U. Albisinni, G. Guglielmi, G. Battista, Ultrasound: Which role in body composition? Eur. J. Radio. vol. 85 (8) (Aug 2016) 1469–1480, https://doi.org/10.1016/j.ejrad.2016.04.005.

[23] M. Clerte, et al., Brown adipose tissue blood flow and mass in obesity: a contrast ultrasound study in mice, J. Am. Soc. Echocardiogr. vol. 26 (12) (Dec 2013) 1465–1473, https://doi.org/10.1016/j.echo.2013.07.015.

[24] R.R. Driskell, C.A. Jahoda, C.M. Chuong, F.M. Watt, V. Horsley, Defining dermal adipose tissue, Exp. Dermatol. vol. 23 (9) (Sep 2014) 629–631, https://doi.org/10.1111/exd.12450.

[25] C.M. Alexander, et al., Dermal white adipose tissue: a new component of the thermogenic response, J. Lipid Res vol. 56 (11) (Nov 2015) 2061–2069, https://doi.org/10.1194/jlr.R062893.

[26] I.L. Kruglikov, P.E. Scherer, Dermal adipocytes: from irrelevance to metabolic targets? Trends Endocrinol. Metab. vol. 27 (1) (Jan 2016) 1–10, https://doi.org/10.1016/j.tem.2015.11.002.

[27] Z. Clerte, et al., Dermal adipose tissue has high plasticity and undergoes reversible dedifferentiation in mice, J. Clin. Invest vol. 129 (12) (Dec 2 2019) 5327–5342, https://doi.org/10.1172/JCI130239.

[28] C.F. Guerrero-Juarez, M.V. Plikus, Emerging nonmetabolic functions of skin fat, Nat. Rev. Endocrinol. vol. 14 (3) (Mar 2018) 163–173, https://doi.org/10.1038/nrendo.2017.162.

[29] K.I. Stanford, R.J. Middelbeek, L.J. Goodyear, Exercise effects on white adipose tissue: beiging and metabolic adaptations, Diabetes vol. 64 (7) (Jul 2015) 2361–2368, https://doi.org/10.2337/db15-0227.

[30] K.I. Stanford, et al., A novel role for subcutaneous adipose tissue in exercise-induced improvements in glucose homeostasis, Diabetes vol. 64 (6) (Jun 2015) 2002–2014, https://doi.org/10.2337/db14-0704.

[31] I. Shimizu, et al., Vascular rarefaction mediates whitening of brown fat in obesity, J. Clin. Invest vol. 124 (5) (May 2014) 2099–2112, https://doi.org/10.1172/JCI71643.

[32] G. Voros, E. Maquoi, D. Demeulemeester, N. Clerx, D. Collen, H.R. Lijnen, Modulation of angiogenesis during adipose tissue development in murine models of obesity, Endocrinology vol. 146 (10) (Oct 2005) 4545–4554, https://doi.org/10.1210/en.2005-0532.

[33] E. Brakenhielm, et al., Angiogenesis inhibitor, TNP-470, prevents diet-induced and genetic obesity in mice, Circ. Res vol. 94 (12) (Jun 25 2004) 1579–1588, https://doi.org/10.1161/01.RES.0000132745.76882.70.

[34] Y.A. An, et al., Angiopoietin-2 in white adipose tissue improves metabolic homeostasis through enhanced angiogenesis, Elife vol. 6 (Mar 29 2017), https://doi.org/10.7554/eLife.24071.

[35] H.K. Sung, et al., Adipose vascular endothelial growth factor regulates metabolic homeostasis through angiogenesis, Cell Metab. vol. 17 (1) (Jan 8 2013) 61–72, https://doi.org/10.1016/j.cmet.2012.12.010.

[36] Y. Xue, X. Xu, X.Q. Zhang, O.C. Farokhzad, R. Langer, Preventing diet-induced obesity in mice by adipose tissue transformation and angiogenesis using targeted nanoparticles, Proc. Natl. Acad. Sci. USA vol. 113 (20) (May 17 2016) 5552–5557, https://doi.org/10.1073/pnas.1603840113.

[37] A. Taruttis, G.M. van Dam, V. Ntziachristos, Mesoscopic and macroscopic optoacoustic imaging of cancer, Cancer Res. vol. 75 (8) (Apr 15 2015) 1548–1559, https://doi.org/10.1158/0008-5472.CAN-14-2522.

[38] L.V. Wang, J. Yao, A practical guide to photoacoustic tomography in the life sciences, Nat. Methods vol. 13 (8) (Jul 28 2016) 627–638, https://doi.org/10.1038/nmeth.3925.

[39] M. Omar, J. Aguirre, V. Ntziachristos, Optoacoustic mesoscopy for biomedicine, Nat. Biomed. Eng. vol. 3 (5) (May 2019) 354–370, https://doi.org/10.1038/s41551-019-0377-4.

[40] V. Ntziachristos, D. Razansky, Molecular imaging by means of multispectral optoacoustic tomography (MSOT), Chem. Rev. vol. 110 (5) (May 12 2010) 2783–2794, https://doi.org/10.1021/cr9002566.

[41] A. Taruttis, V. Ntziachristos, Advances in real-time multispectral optoacoustic imaging and its applications, Nat. Photonics vol. 9 (4) (2015) 219–227, https://doi.org/10.1038/nphoton.2015.29.

[42] J. Reber, et al., Non-invasive Measurement of Brown Fat Metabolism Based on Optoacoustic Imaging of Hemoglobin Gradients, Cell Metab. vol. 27 (3) (Mar 6 2018) 689–701 e4, https://doi.org/10.1016/j.cmet.2018.02.002.

[43] Y. Li, et al., Secretin-Activated Brown Fat Mediates Prandial Thermogenesis to Induce Satiation, Cell vol. 175 (6) (Nov 29 2018) 1561–1574 e12, https://doi.org/10.1016/j.cell.2018.10.016.

[44] A. Buehler, G. Diot, T. Volz, J. Kohlmeyer, V. Ntziachristos, Imaging of fatty tumors: appearance of subcutaneous lipomas in optoacoustic images, J. Biophoton. vol. 10 (8) (Aug 2017) 983–989, https://doi.org/10.1002/jbio.201600274.

[45] H. He, et al., Fast raster-scan optoacoustic mesoscopy enables assessment of human melanoma microvasculature in vivo, Nat. Com. vol. 13 (1) (2022), https://doi.org/10.1038/s41467-022-30471-9.

[46] R. Ma, A. Taruttis, V. Ntziachristos, D. Razansky, Multispectral optoacoustic tomography (MSOT) scanner for whole-body small animal imaging, Opt. Express vol. 17 (24) (Nov 23 2009) 21414–21426, https://doi.org/10.1364/OE.17.021414.

[47] H. He, et al., Opening a window to skin biomarkers for diabetes stage with optoacoustic mesoscopy, Light Sci. Appl. vol. 12 (1) (Sep 18 2023) 231, https://doi.org/10.1038/s41377-023-01275-3.

[48] D. Razansky, A. Buehler, V. Ntziachristos, Volumetric real-time multispectral optoacoustic tomography of biomarkers, Nat. Protoc. vol. 6 (8) (Aug 2011) 1121–1129, https://doi.org/10.1038/nprot.2011.351.

[49] C. Ruehl-Fehlert, et al., Revised guides for organ sampling and trimming in rats and mice–part 1, Exp. Toxicol. Pathol. vol. 55 (2-3) (Sep 2003) 91–106.

[50] J. Aguirre, et al., Precision assessment of label-free psoriasis biomarkers with ultra-broadband optoacoustic mesoscopy, Nat. Biomed. Eng. vol. 1 (5) (May 2017) 0068.

[51] M. Omar, J. Gateau, V. Ntziachristos, Raster-scan optoacoustic mesoscopy in the 25–125 MHz range, Opt. Lett. vol. 38 (14) (Jul 15 2013) 2472–2474, https://doi.org/10.1364/OL.38.002472.

[52] M. Schwarz, N. Garzorz-Stark, K. Eyerich, J. Aguirre, V. Ntziachristos, Motion correction in optoacoustic mesoscopy, Sci. Rep. vol. 7 (1) (Sep 4 2017) 10386, https://doi.org/10.1038/s41598-017-11277-y.

[53] S.J. Chiu, X.T. Li, P. Nicholas, C.A. Toth, J.A. Izatt, S. Farsiu, Automatic segmentation of seven retinal layers in SDOCT images congruent with expert manual segmentation, Opt. Express vol. 18 (18) (Aug 30 2010) 19413–19428, https://doi.org/10.1364/OE.18.019413.

[54] D. Bianconi, et al., Microvascular density assessed by CD31 predicts clinical benefit upon bevacizumab treatment in metastatic colorectal cancer: results of the PassionATE study, a translational prospective Phase II study of capecitabine and irinotecan plus bevacizumab followed by capecitabine and oxaliplatin plus bevacizumab or the reverse sequence in patients in mCRC, Ther. Adv. Med Oncol. vol. 12 (2020) 1758835920928635, https://doi.org/10.1177/1758835920928635.

[55] I. Kasza, D. Hernando, A. Roldan-Alzate, C.M. Alexander, S.B. Reeder, Thermogenic profiling using magnetic resonance imaging of dermal and other adipose tissues, JCI Insight vol. 1 (13) (Aug 18 2016) e87146, https://doi.org/10.1172/jci.insight.87146.

[56] A. Berezhnoi, et al., Optical features of human skin revealed by optoacoustic mesoscopy in the visible and short-wave infrared regions, Opt. Lett. vol. 44 (17) (Sep 1 2019) 4119–4122, https://doi.org/10.1364/OL.44.004119.

[57] A.B.E. Attia, et al., A review of clinical photoacoustic imaging: current and future trends, Photoacoustics vol. 16 (Dec 2019) 100144, https://doi.org/10.1016/j.pacs.2019.100144.

Shan Huang received her Ph.D. in life science from the Hong Kong University of Science and Technology, China, followed by postdoctoral positions at the German Cancer Research Center and the Institute for Biological and Medical Imaging at the Helmholtz Zentrum in Munich, Germany. Afterwards, she established 'Biomarker' research group in the Chair for Biological Imaging at the Technical University Munich. Her research focused on identifying novel biomarkers using photoacoustic technologies. Currently, she is a clinical scientist at Philips.

Hailong He received his Ph.D. in Faculty of Electrical Engineering, Technical University of Munich, 2018. Afterwards, he worked as a postdoc researcher at the Institute of Biological and Medical Imaging (IBMI) at the Helmholtz Zentrum München. Since 2021, he works as Group Leader at IBMI. His research interests focus on the development of optoacoustic imaging techniques for clinical applications.

Robby Zachariah Tom received his Ph.D from the department of Molecular Medicine, Karolinska Institutet Sweden. He is currently a Post Doctoral Research Fellow working with Prof. Susanna Hofmann at Medizinische Klinik und Poliklinik IV, Ludwig-Maximilians-Universität, Munich. His research work mainly focuses on understanding the role of sex difference and exercise in the regulation of energy homeostasis to uncover novel drug targets to treat metabolic diseases.

Sarah Glasl is a biological-technical Assistant. Since 2009, she has been employed at the Institute for Biological and Medical Imaging at Helmholtz Zentrum München and the Chair of Biological Imaging at the Technical University Munich. She contributes to high impact research in the field of biological imaging. Her expertise lies in the development and validation of animal models and experimental protocols for opto-acoustic, fluorescence, and non-linear imaging techniques.

Pia Anzenhofer started her career as a Biological Technical Assistant in scientific research in 2009. She began her professional journey at LMU, specialising in histology, tissue preparation, and tissue staining. Since 2017, Pia has worked at the Institute of Biological and Medical Imaging at Helmholtz Zentrum Munich, collaborating closely with the Chair of Medical Imaging at TUM. In her role, she supported EU-funded projects at the institutes and adeptly managed animal models, executed intricate handling operations, and specialised in cell culture work. Her proficiency extends across a broad spectrum of technical skills crucial for the success of complex research projects.

After receiving his Diploma in Biology from the Ruhr University Bochum, Germany, Andre conducted his Ph.D. studies at the Max Planck Institute for Biophysical Chemistry, Göttingen, Germany, in the group of Nobel Laureate Stefan Hell where he was pivotal in pioneering the field of photo-switchable proteins for super-resolution imaging. After receiving his Ph.D. from the Ruprecht-Karls University, Heidelberg, in 2008 Andre moved for a postdoctoral stay to the Max Planck Institute for Developmental Biology, Tübingen, Germany, where he worked on computer aided protein engineering. During his time in Tübingen Andre spend time as a guest researcher at the HHMI research campus Janelia Farm, USA. In 2015 Andre moved to Munich to start the CellEngineering group at the Institute for Biological and Medical Imaging at Helmholtz Munich focusing on advancing the field of reporters and sensors for innovative optical imaging methods like optoacoustic imaging or super-resolution fluorescence microscopy. Since 2024, Andre is full professor at the University of Regensburg.

Susanna Hofmann received her M.D. from the University of Padova, Italy, followed by a residency at the Department for Endocrinology of the LMU University, Munich. She was awarded postdoctoral fellowship and career development awards at Mount Sinai School of Medicine, Albert Einstein College of Medicine in NYC and University of Cincinnati. After that she became an Instructor and following an Assistant Professor at the Department for Endocrinology of the University of Cincinnati, Cincinnati, USA. Currently she is the Head of the Division "Women and Diabetes" at the Institute for Diabetes and Regeneration of the Helmholtz Center for Health Research in Munich as well as a Professor for Lipidology and Metabolic Disease at the University Hospital of the LMU University in Munich. Her work focuses on the identification of novel individual biomarkers for the prevention, prognosis, and treatment response of cardiometabolic disease.

Vasilis Ntziachristos received his Ph.D. in electrical engineering from the University of Pennsylvania, USA, followed by a postdoctoral position at the Center for Molecular Imaging Research at Harvard Medical School. Afterwards, he became an Instructor and following an Assistant Professor and Director at the Laboratory for Bio-Optics and Molecular Imaging at Harvard University and Massachusetts General Hospital, Boston, USA. Currently, he is the Director of the Institute for Biological and Medical Imaging at the Helmholtz Zentrum in Munich, Germany, as well as a Professor of Electrical Engineering, Professor of Medicine and Chair for Biological Imaging at the Technical University Munich. His work focuses on novel innovative optical and optoacoustic imaging modalities for studying biological processes and diseases as well as the translation of these findings into the clinic.